



Development and validation of an asymptotic solution for a two-phase Stefan problem in a droplet subjected to convective boundary condition

Saad Akhtar, Minghan Xu, Agus P. Sasmito*

Department of Mining and Materials Engineering, McGill University, Montreal, Canada H3A 0E8

ARTICLE INFO

Keywords:

Perturbation series solution
Asymptotic expansion
Droplet freezing
Two-phase Stefan problem
Enthalpy–porosity method

ABSTRACT

Droplet solidification is governed by classical Stefan problems which have been commonly treated as a single-phase problem by the majority of the studies in the literature. This approach, however, is unable to capture the initial temperature and the start of freezing time correctly. The treatment of two-phase Stefan problem in spherical coordinates is limited. No known exact solution exists, albeit numerical solutions and asymptotics have proven to be useful. We present a singular perturbation solution in the limit of low Stefan number and arbitrary Biot number for the two-phase Stefan problem in a finite spherical domain. An asymptotic solution is developed for a droplet at a non-freezing initial temperature subjected to a convective boundary condition at the surface. The solution is developed for both long-time and short-time scales. The results from asymptotic expansion method are validated with the experimental results in the literature and are further verified by a numerical model of a freezing droplet using enthalpy–porosity method. The sensitivity of the asymptotic solution to the droplet initial temperature, Biot number, and Stefan number has also been studied. The results indicate that the solution from perturbation series and enthalpy–porosity method agrees to within 1%–10% for temperature profile and overall freezing times over a wide range of practical values for initial temperature, Stefan and Biot numbers for the application of spray freezing. Our perturbation series solution is also able to capture the effect of initial temperature on the overall freezing time of the droplet.

1. Introduction

Solid–liquid phase-change process in a sphere has widespread applications in atmospheric sciences [1,2], underground mine ventilation (spray freezing heating and cooling) [3,4], pharmaceuticals (spray crystallization) [5,6], food processing industry [7,8], and phase-change materials [9,10], thus making it an important problem to investigate. Stefan problem has been extensively used in the literature to study the phase-change behavior in pure materials and binary alloys. Several analytical [11–14], numerical [7,15–18] and experimental studies [7, 19–23] have been undertaken in the literature to investigate the thermal and the phase-change behavior in a droplet which is of critical importance for efficient design in many engineering applications. Analytical, semi-analytical and hybrid analytical–numerical methods have the advantage of allowing the engineers and computational scientists to expedite the design process by using quick-to-obtain solutions from such approaches.

Stefan problem has been extensively tackled for a variety of geometrical configurations and material types. For infinite and semi-infinite domains in the planar case, exact solutions by similarity transforma-

tions exist and have been well documented [24–27]. However, the Stefan problem in spherical and cylindrical configuration cannot be closed analytically to the best of our knowledge. In such configurations it is convenient to use asymptotics, hybrid analytical–numerical, and numerical methods to get approximate solutions.

Perturbation series analysis for Stefan problem has proven to be an effective and versatile tool in developing accurate solutions for a wide variety of boundary conditions. The method, explored in depth by Nayfeh [28] in solid mechanics, Van Dyke in fluid mechanics [29] and Aziz [30] in heat transfer applications, uses a power series expanded around a small (perturbation) parameter to obtain approximate solutions to the governing partial differential equations (PDEs). Perturbation techniques can be mainly categorized as parameter perturbation and coordinate perturbation. This distinction depends on the perturbation parameter selected. Each of these expansions can be further categorized into regular and singular perturbations. Regular perturbation is used if the expansion is uniformly valid, whereas singular perturbation is required for the cases where the expansion blows up in a certain time and/or length scales [30,31]. As pointed by several studies in the literature [12,14,32,33], the inwards droplet freezing

* Corresponding author.

E-mail addresses: saad.akhtar@mail.mcgill.ca (S. Akhtar), minghan.xu@mail.mcgill.ca (M. Xu), agus.sasmito@mcgill.ca (A.P. Sasmito).

Nomenclature

\dot{q}	Heat flux [W/m ²]
Bi	Biot number
Fo	Fourier number
Gr	Grashoff number
Nu	Nusselt number
Pr	Prandtl number
Re	Reynolds number
Ri	Richardson number
Sc	Schmidt number
Sh	Sherwood number
Ste	Stefan number
a	Droplet radius [m]
c	Specific heat [kJ/(kg K)]
D_{ab}	Mass diffusivity [m ² /s]
H	Total enthalpy [J/kg]
h	Heat transfer coefficient [W/(m ² K)]
k	Thermal conductivity [W/(m K)]
L	Latent heat of fusion [kJ/K]
l	Length [m]
P	Pressure [Pa]
r	Radial coordinate [m]
r_i	Interface location [m]
T	Temperature [K]
t	Time [s]
v	Air velocity [m]

Greek Symbols

α	Ratio of thermal diffusivity
β	Eigenvalues
ϵ	Emissivity
η	Dimensionless coordinate in liquid phase
γ	Liquid fraction
μ	Dynamic Viscosity [kg/(m s)]
ρ	Density [kg/m ³]
σ	Boltzmann Constant [m ² kg/(s ² K)]
T	Dimensionless stretched time
τ	Dimensionless time
θ	Dimensionless temperature
ξ	Dimensionless coordinate in solid phase
ζ	Dimensionless interface location

Superscripts and subscripts

*	Dimensionless coordinate
-	Inner expansion
∞	Free stream
c	Characteristic
d	Droplet
eq	Equivalent
f	Fusion
i	Initial
l	Liquid
liq	Liquidus
n	Order of perturbation
s	Solid
sol	Solidus
sw	Saturated water
v	Vapor

problem has singularity near the center of the droplet. Thus, the singular perturbation approach is most suitable to obtain uniformly valid solutions.

The single-phase Stefan problem in a sphere has been mostly studied in the literature by the singular perturbation method. Through the methods of strained coordinates [34–36] and matched asymptotics [13,33,37,38] numerous studies have investigated the interface movement and freezing times for several boundary conditions. Pedroso & Domoto [34] used the method of strained coordinates to obtain the temperature distribution and freezing times for both outwards and inwards solidification in a sphere subjected to constant wall temperature. Prud'Homme [35] and Parang et al. [36] also used the same technique in a sphere for constant temperature, heat flux, convective and radiative boundary conditions. The method of strained coordinates is a robust singular perturbation technique to obtain uniformly valid solution. However, the method yields incorrect results for times approaching the final freezing time as pointed out by McCue et al. [12]. Hence, in this study the method of matched asymptotics is preferred to tackle singularity occurred at the initial time.

Matched asymptotics has been widely applied to the Stefan problem owing to its physically intuitive deconstruction of the spatial and temporal scales in a finite, radially symmetric domain. The approach requires obtaining separate solutions for each of the spatio-temporal layer and then matching the solutions at the interface of those layers using Van Dyke's rule [29] or other matching principles. Riley et al. [13] estimated the solidification time, interface motion and temperature field in a sphere for the single-phase Stefan problem. The analysis was further refined by Soward [37], and Sewartson & Waechter [38]. Another study by Tabakova et al. [33] analyzed the Stefan problem in a sphere with convective boundary condition and recalescence, the latter of which was incorporated through defining an effective latent heat.

While the single-phase Stefan problem in a sphere has received a lot of analytical, semi-analytical and numerical treatment in the literature, the perturbation analysis for two-phase Stefan problem has received limited attention. Majority of the studies justify using single-phase Stefan problem because of the weak dependency of liquid phase temperature gradient on the interface propagation for low Stefan numbers (latent heat dominated). This assumption is somewhat justified if the initial temperature of the droplet is close to freezing temperature [12]. However, as the recent results presented by Dehghani et al. [16] show, for high initial droplet temperature the thermal gradients in the liquid phase can impact the interface location and overall freezing times. Thus, it is important to consider temperature gradients in both solid and liquid phases for such conditions.

Jiji & Weinbaum [14] were amongst the first to apply singular perturbation series to a two-phase Stefan problem using boundary fixing transformation. Their analytical model was applied to concentric cylindrical geometry with isothermal and insulation boundary condition at the inner surface. The model took into account the effect of initial droplet temperature on the temperature field and freezing times. Kucera & Hill, [39] extended the analysis to spheres and computed the radial temperature profile and interface motion for both melting and freezing problems. McCue et al. [12] developed an extensive spatio-temporal framework to analyze the two-phase Stefan problem for constant temperature boundary condition. Their notable contribution to the previous studies was the introduction of a very small time scale to study the coupling of liquid and solid phases and identifying the time scales in which those phases decouple. More recently, Planella et al. [40] extended the analysis of McCue et al. [12] and incorporated the effect of impurities and constitutional supercooling on the solidification process. They presented a detailed break down of different time and length scales that are critical to analyzing the freezing behavior.

Based on the review of the work done on two-phase Stefan problems, there are several gaps in the literature that need to be addressed. Firstly, to the best of our knowledge, there is no current study that asymptotically investigates the effect of convective boundary condition

for a two-phase Stefan problem for finite, symmetric, spherical domain. While Tabakova et al. [33] did devise the asymptotic analysis for a finite sphere under the convective boundary condition, their solution was for a single-phase Stefan problem with constant density assumption in both phases. They also did not take into account the effect of initial temperature, supercooling, and phase-dependent thermophysical properties on freezing time. Jiji & Weinbaum [14], Kucera & Hill [39], McCue et al. [12] and Planella et al. [40] considered the constant temperature boundary condition on the surface of the sphere whereas most of these studies did not consider the impact of initial temperature and convective boundary condition on the overall freezing time of a sphere. Our study fills these gaps by developing and verifying a perturbation series solution for a two-phase Stefan problem subjected to a convective boundary condition for variable initial droplet temperature, and phase-dependent thermophysical properties.

Secondly, the perturbation series solution developed in the literature for droplet freezing are rarely validated. Here, we validate our perturbation series solution with experimental results from Hindmarsh et al. [7]. We extend the approach introduced by Jiji & Weinbaum [14] to the spherical finite geometry with mixed boundary condition at the surface. The study presents a unique approach to model different freezing stages of a droplet and obtain a uniformly valid solution. The results from the analytical model are verified with results from the fixed-grid enthalpy porosity numerical model [41] using a finite volume discretization approach and numerical results from Dehghani et al. [16]. The temperature profile and freezing times are also validated with the experimental results of Hindmarsh et al. [7].

The outline of the paper is as follows. In Section 2, we present the governing equations, boundary conditions, underlying assumptions in our model and modeling analysis for three different stages of a droplet freezing, namely liquid sensible cooling, phase-change and solid sub-cooling. The phase-change modeling approach presented in this section employs a boundary fixing transformation to address the non-linearity in the interface boundary condition. In Section 3, the perturbation series expansion is developed for a small Stefan approximation and the response of the governing equations for quasi-steady (long-time scale) and quasi-stationary (short-time scale) is studied in depth. Section 4 presents the governing equations, boundary conditions, thermal properties and numerical methodology for the enthalpy–porosity technique [41] used in our numerical model. In Section 5, we verify and validate our results and further study their usefulness for the application of spray freezing for different cases of initial temperature, Biot and Stefan numbers. Lastly, Section 6 presents the main conclusion of the study and highlights the usefulness of the results obtained while outlining the future directions for the possible extension of this work.

2. Analytical treatment of droplet solidification

This section presents the physical and mathematical model along with the detailed development of perturbation series solution for the solidification problem in a droplet. This study considers the spatial gradients in both phases and thus requires assumptions for mathematical simplification. The following assumptions have been made to simplify the analytical analysis:

- (i) The spatial gradients for the analytical solution are assumed to be in radial direction only (i.e., droplet symmetry);
- (ii) Phase-dependent thermophysical properties are used for solid and liquid phases. However, the temperature dependency of the properties within each phase is neglected;
- (iii) Modeling of nucleation and recalescence dynamics is not included;
- (iv) The conditions for equilibrium freezing model is assumed (i.e., the temperature at the interface is considered to be constant $T_f = 273.15$ K);
- (v) A sharp interface is assumed between liquid and solid phases; and

Table 1

Thermo-physical properties for the base case used for validation [7]. Air properties are evaluated at 258.15 K.

Property	Value	Unit
ρ_{air}	1.125	kg/m ³
k_{air}	2.3125×10^{-2}	W/(m K)
μ_{air}	1.68×10^{-5}	kg/(m s)
h_{eq}	127	W/(m ² K)
$c_{p,l}$	4.2	kJ/(kg K)
$c_{p,s}$	2.1	kJ/(kg K)
k_l	0.6	W/(m K)
k_s	2.22	W/(m K)
α_l	1.362×10^{-7}	m ² /s
α_s	1.182×10^{-6}	m ² /s
T_i	280.85	K
T_f	273.15	K
T_∞	258.15	K
L	334	kJ/(kg K)
a	0.78	mm
v	0.54	m/s
Ste	0.092	–
Bi	0.059	–

- (vi) Natural convection inside the melt is neglected since the Richardson number, $Ri = Gr/Re^2 \ll 1$, where Gr is the Grashoff number and Re is Reynolds number.

The subsequent section presents the governing equation and boundary conditions that form the basis of this problem.

2.1. Governing equations

The freezing problem for a droplet is governed by transient heat conduction equation in spherical coordinates. For uniform boundary conditions, the heat transfer gradients in azimuthal and polar directions can be ignored and the resulting one-dimensional (1-D) transient heat conduction equation is given as follows:

$$\frac{\partial T_l}{\partial t} = \alpha_l \left(\frac{\partial^2 T_l}{\partial r^2} + \frac{2}{r} \frac{\partial T_l}{\partial r} \right), \quad (1)$$

$$\frac{\partial T_s}{\partial t} = \alpha_s \left(\frac{\partial^2 T_s}{\partial r^2} + \frac{2}{r} \frac{\partial T_s}{\partial r} \right). \quad (2)$$

The schematic diagram for the phase-change problem is given in Fig. 1. This study focuses on the spray freezing application, where the thermal interaction between the droplet and the surrounding environment is primarily dominated by forced convection on the external surface.

Droplet freezing is characterized into three sequential stages to assist with the mathematical analysis and physical interpretation of the results. These three stages namely liquid sensible cooling, phase-change and solid sub-cooling are analyzed further in the following subsections. The boundary conditions for Eqs. (1), (2) depend on the freezing stage and are thus presented in the relevant subsections.

For the validation and verification of these results, we have chosen the base case of the experimental study of Hindmarsh et al. [7], which considers the convective freezing of a liquid droplet with a diameter of 780 μ m in a sub-cooled air at 258.15 K. The thermal properties and operating conditions are listed in detail in Table 1.

2.2. Liquid sensible cooling

The temperature response in the solid and liquid domain far from the moving interface can be solved using transient heat conduction equation. A similar concept of demarcation of a finite phase-change domain in spherical coordinates was proposed by McCue et al. [12] and further formalized by Planella et al. [40] who divided the domain into different regions based on their proximity to the interface (boundary layers) for different time scales. For the region and times far from

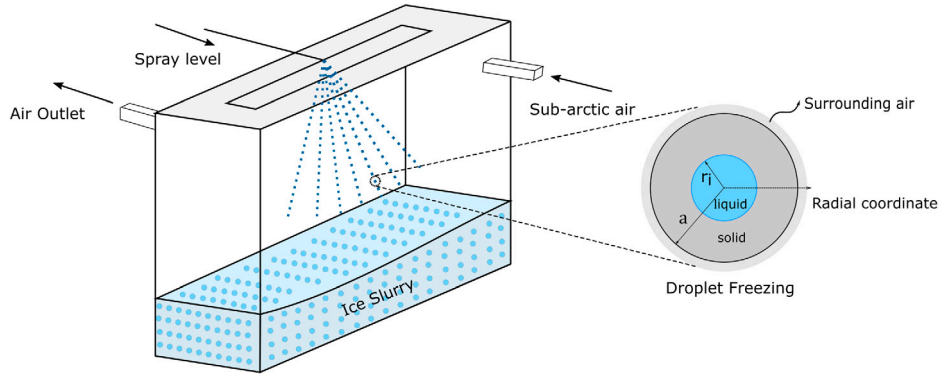


Fig. 1. Schematic of the droplet subjected to convective boundary condition during the spray freezing process.

phase-change, the heat transfer in the liquid phase is governed by the 1-D transient heat conduction equation. Thus, at an initial temperature $T(r, 0) = T_i$, Eq. (1) is subjected to the Boundary Conditions (BCs) and the Initial Condition (IC) laid down as follows:

$$-k_l \left. \frac{\partial T_l}{\partial r} \right|_{(a,t)} = h_{eq}(T_l(a,t) - T_\infty), \quad (3a)$$

$$\left. \frac{\partial T_l}{\partial r} \right|_{(0,t)} = 0, \quad (3b)$$

$$T_l(r, 0) = T_i. \quad (3c)$$

For a more concise analysis, the independent variables in Eqs. (1) and (3) should be non-dimensionalized. Using $\theta = (T - T_\infty)/(T_i - T_\infty)$ as the dimensionless temperature profile, $r^* = r/a$ as the dimensionless radial coordinate, and $Fo = \alpha_l/a^2$ as the dimensionless time for the liquid phase we get the following set of equations

$$\frac{\partial \theta}{\partial Fo} = \left(\frac{\partial^2 \theta}{\partial r^{*2}} + \frac{2}{r^*} \frac{\partial \theta}{\partial r^*} \right), \quad (4)$$

with the BCs and IC transforming as

$$\left. \frac{\partial \theta}{\partial r^*} \right|_{(1,Fo)} = -Bi\theta(1, Fo), \quad (5a)$$

$$\left. \frac{\partial \theta}{\partial r^*} \right|_{(0,Fo)} = 0, \quad (5b)$$

$$\theta_l(1, 0) = \theta_i. \quad (5c)$$

In Eq. (5a), $Bi = h_{eq}a/k$, is the Biot number that quantifies the ratio of conductive thermal resistance to convective thermal resistance. The solution to the Eq. (4) subjected to the conditions in Eq. (5) is well known in the heat transfer literature [42] and is of the following form:

$$\theta = \sum_{n=1}^{\infty} A_n e^{-\beta_n^2 Fo} f_n(\beta_n, r^*), \quad (6a)$$

$$A_n(\beta_n) = \frac{2(\sin \beta_n - \beta_n \cos \beta_n)}{\beta_n - \sin \beta_n \cos \beta_n}, \quad (6b)$$

$$f_n(\beta_n, r^*) = \frac{\sin[\beta_n r^*]}{\beta_n r^*}. \quad (6c)$$

The eigenvalues β_n are governed by the following transcendental equation:

$$\beta \cos \beta + (Bi - 1) \sin \beta = 0. \quad (7)$$

For an accurate estimation of the temperature profile, the number of eigenvalues should be high. We have used the Scipy module [43] in Python to compute the first 50 eigenvalues of the transcendental equation given by Eq. (7). The model presented above can also be used to capture supercooling, provided that we have *a priori* knowledge of the nucleation temperature from experiments.

2.3. Phase change

The governing equations for the phase-change process during the freezing of a droplet are the same as given in Eqs. (1), (2). However, because of the inward moving interface, the domain of both liquid and solid phase is dynamic. The schematic is given in Fig. 1. For this stage the solid and liquid phases coexist and for the problem of inwards freezing only the solid surface is in contact with the cold environment. The BCs and the ICs for Eqs. (1), (2) are as follows. For the liquid phase:

$$\left. \frac{\partial T_l}{\partial r} \right|_{(0,t)} = 0, \quad (8a)$$

$$T_l(r_i, t) = T_f, \quad (8b)$$

$$T_l(r, 0) = T_i > T_f. \quad (8c)$$

For the solid phase:

$$-k_s \left. \frac{\partial T_s}{\partial r} \right|_{(a,t)} = h_{eq}(T_s(a,t) - T_\infty), \quad (9a)$$

$$T_s(r_i, t) = T_f. \quad (9b)$$

To resolve the motion of the interface between liquid and solid, the interface energy balance must be taken into account. For a two-phase Stefan problem the interface energy balance yields

$$k_s \left. \frac{\partial T_s}{\partial r} \right|_{(r_i,t)} - k_l \left. \frac{\partial T_l}{\partial r} \right|_{(r_i,t)} = \rho L \frac{dr_i}{dt}, \quad (10)$$

which is subjected to the initial condition

$$r_i(0) = a. \quad (11)$$

It is important to mention here that in the Eq. (8c), T_i is assumed to be spatially constant for this study. This assumption is undertaken to aid with the perturbation analysis presented in Section 3. In later sections it will be shown that this assumption allows us to capture the effect of initial temperature on the interface motion as given by Eq. (75) and leads to a good comparison with the experimental temperature profile illustrated in Fig. 5.

2.3.1. Non-dimensionalization and immobilization

Eqs. (1), (2) in conjunction with the BCs and the IC given in Eqs. (8), (9), govern the solution to the two-phase Stefan problem. It is analytically feasible to re-define the moving boundary problem into a fixed boundary problem by transforming the coordinates. For this transformation we need to define the dimensionless parameters first

$$\theta_s = \frac{T_s(r, t) - T_\infty}{T_f - T_\infty}, \quad \theta_l = \frac{k_l(T_l(r, t) - T_f)}{k_s(T_f - T_\infty)}, \quad \alpha = \frac{\alpha_s}{\alpha_l}, \quad (12)$$

$$Ste = \frac{c_{p,s}(T_f - T_\infty)}{L}, \quad Bi = \frac{ha}{k_s}, \quad \tau = \frac{Ste \alpha_s t}{a^2}.$$

The immobilized and dimensionless coordinates used for the transformation are defined as

$$\xi = \frac{a - r}{a - r_i(t)}, \quad \eta = \frac{r_i(t) - r}{r_i(t)}, \quad \zeta = \frac{a - r_i(t)}{a}. \quad (13)$$

Substituting these parameters in Eqs. (1), (2) we get:

$$\begin{aligned} \frac{\partial^2 \theta_s}{\partial \xi^2} - \frac{2\zeta}{1 - \zeta\xi} \frac{\partial \theta_s}{\partial \xi} &= \text{Ste} \left[\zeta^2 \frac{\partial \theta_s}{\partial \tau} - \xi\zeta \frac{\partial \theta_s}{\partial \xi} \frac{d\zeta}{d\tau} \right], \quad 0 < \xi < 1 \\ \frac{\partial^2 \theta_l}{\partial \eta^2} - \frac{2}{1 - \eta} \frac{\partial \theta_l}{\partial \eta} &= \text{Ste}\alpha \left[(1 - \zeta)^2 \frac{\partial \theta_l}{\partial \tau} - (1 - \eta)(1 - \zeta) \frac{\partial \theta_l}{\partial \eta} \frac{d\zeta}{d\tau} \right], \quad 0 < \eta < 1. \end{aligned} \quad (14)$$

The BCs and IC given in Eqs. (8), (9) transform into

$$\begin{aligned} \frac{1}{\zeta} \frac{\partial \theta_s}{\partial \xi} \Big|_{(0,\tau)} - \text{Bi}\theta_s(0, \tau) &= 0, \quad \theta_s(1, \tau) = 1, \\ \frac{\partial \theta_l}{\partial \eta} \Big|_{(1,\tau)} &= 0, \quad \theta_l(0, \tau) = 0, \\ \theta_l(\eta, 0) &= \theta_i, \quad \theta_i = \frac{k_l(T_i - T_\infty)}{k_s(T_f - T_\infty)}. \end{aligned} \quad (15)$$

The resulting interface energy balance equation and the boundary condition is given by

$$\begin{aligned} \frac{\partial \theta_s}{\partial \xi} \Big|_{(1,\tau)} - \frac{\zeta}{1 - \zeta} \frac{\partial \theta_l}{\partial \eta} \Big|_{(0,\tau)} &= \zeta \frac{d\zeta}{d\tau}, \\ \zeta(0) &= 0. \end{aligned} \quad (16)$$

2.4. Solid sub-cooling

After the core has completely frozen, the solidified droplet still undergoes sub-cooling till it reaches in equilibrium with its surrounding temperature. To get an idea of whether resolving the spatial gradients within the solidified droplet (ice) is important or not, we compute Biot number. Using the values in Table 1, the Biot number comes out to be less than 0.1, which allows us to use the lumped heat capacitance model. For a droplet with uniform temperature subjective to convective heat transfer on the boundary, the lumped heat capacitance model yields:

$$\frac{T - T_\infty}{T_0 - T_\infty} = e^{-(3h_{eq}/\rho a c_p)t}. \quad (17)$$

where, T_0 is the initial temperature at the start of solid sub-cooling stage, which would be the freezing temperature T_f .

3. Perturbation solution for phase-change

The Eqs. (14)–(16), though in fixed coordinates, are non-linear PDEs. This precludes the possibility of having a closed form exact solution for this problem. However, a series solution approximation can yield some insightful results. This section extends the asymptotic expansion approach outlined by Jiji and Weinbaum [14] to apply quasi-steady-state approximation (outer expansion) and quasi-stationary approximation (inner expansion) for the governing equations of solid, liquid and interface motion. The inner expansion uses a stretched time coordinate, $T = \alpha_s t/a^2 = \tau/\text{Ste}$ which unlike the outer expansion captures the small time scale effects and is valid as $\tau \rightarrow 0$.

The perturbation series expansion requires the following steps:

- (i) Non-dimensionalize the governing equations and assess the order of magnitude of different terms;
- (ii) Identify a perturbation parameter;
- (iii) Assume the solution to the unknown quantities to be an asymptotic series of the perturbation parameter;
- (iv) Substitute the series solution in the governing equations;
- (v) Equate the coefficients of each power of the perturbation parameter on both sides of the equation; and

- (vi) Solve the subsequent set of equations to get the coefficients of the series solution.

Analyzing the Eqs. (14)–(16), Stefan number is identified as the perturbation parameter. The series solution for θ_s , θ_l , and ζ can be presented as

$$\begin{aligned} \theta_s(\xi, \tau; \text{Ste}) &\sim \sum_{n=0}^N (\text{Ste})^{n/2} \theta_{sn}(\xi, \tau), \\ \theta_l(\eta, \tau; \text{Ste}) &\sim \sum_{n=0}^N (\text{Ste})^{n/2} \theta_{ln}(\eta, \tau), \\ \zeta_l(\tau; \text{Ste}) &\sim \sum_{n=0}^N (\text{Ste})^{n/2} \zeta_n(\tau). \end{aligned} \quad (18)$$

3.1. Outer expansion

The outer expansion captures the long time behavior in our series expansion solution. Hence, we do not alter the time scale as presented in Eq. (18) and substitute it in the Eqs. (14)–(16) as is. Terms of up to first order are calculated in this expansion where possible. The series solution would be of the form:

$$\begin{aligned} \theta_l(\eta, \tau) &= \theta_{l0} + \theta_{l1} \text{Ste}^{1/2} + \text{H.O.T.}, \\ \theta_s(\xi, \tau) &= \theta_{s0} + \theta_{s1} \text{Ste}^{1/2} + \text{H.O.T.}, \\ \zeta(\tau) &= \zeta_0 + \zeta_1 \text{Ste}^{1/2} + \text{H.O.T.} \end{aligned} \quad (19)$$

In the text that follows we aim to solve for the coefficients in Eq. (19).

3.1.1. Zero-order

The zero-order term in Eq. (19) is substituted in Eq. (14)–(16). Comparing the terms of equal power of Ste^0 on left and right hand side of the equations for solid, liquid and the interface equations, the zero-order approximation yields the following. For the liquid phase we get:

$$\begin{aligned} \frac{\partial^2 \theta_{l0}}{\partial \eta^2} - \frac{2}{1 - \eta} \frac{\partial \theta_{l0}}{\partial \eta} &= 0 \quad 0 < \eta < 1, \\ \frac{\partial \theta_{l0}}{\partial \eta} \Big|_{(0,\tau)} &= 0, \quad \theta_{l0}(0, \tau) = 0. \end{aligned} \quad (20)$$

Solid phase equations become:

$$\begin{aligned} \frac{\partial^2 \theta_{s0}}{\partial \xi^2} - \frac{2\zeta_0}{1 - \zeta_0\xi} \frac{\partial \theta_{s0}}{\partial \xi} &= 0 \quad 0 < \xi < 1, \\ \frac{1}{\zeta_0} \frac{\partial \theta_{s0}}{\partial \xi} \Big|_{(0,\tau)} - \text{Bi}\theta_{s0}(0, \tau) &= 0, \quad \theta_{s0}(1, \tau) = 1. \end{aligned} \quad (21)$$

Interface equations yield:

$$\begin{aligned} \frac{\partial \theta_{s0}}{\partial \xi} \Big|_{(1,\tau)} - \frac{\zeta_0}{1 - \zeta_0} \frac{\partial \theta_l}{\partial \eta} \Big|_{(0,\tau)} &= \zeta_0 \frac{d\zeta_0}{d\tau}, \\ \zeta_0(0) &= 0. \end{aligned} \quad (22)$$

Solving the Eqs. (20)–(22) in Mathematica we get the following solution. For the liquid phase it yields:

$$\theta_{l0} = 0. \quad (23)$$

For the solid phase we get:

$$\theta_{s0} = \frac{(\zeta_0 - 1)(1 + \zeta_0\xi(\text{Bi} - 1))}{(1 + (\text{Bi} - 1)\zeta_0)(\zeta_0\xi - 1)}. \quad (24)$$

Using Eqs. (23) and (24) with (22), the interface equation yields:

$$\begin{aligned} \text{Bi}(\xi - 1)^2 \ln(1 - \zeta_0) + (-1 + \text{Bi}(\xi - 1)^2)\zeta_0 + \\ \frac{1}{2}(2 + \text{Bi}(\xi - 2))\xi\zeta_0^2 + \frac{1}{3}(\text{Bi} - 1)\xi^2\zeta_0^3 &= -\text{Bi}\tau + C_1. \end{aligned} \quad (25)$$

To determine the constant C_1 in Eq. (25) we need to assume a polynomial expression for the outer interface solution, ζ . Since ζ is the function of time only, it can be written as:

$$\zeta_0 = a_0 + a_1(\tau)^{1/2} + a_2(\tau). \quad (26)$$

The initial condition for the interface, $\zeta_0(0) = 0$, implies that $a_0 = 0$. Substituting Eq. (26) in Eq. (25) and equating the coefficients of equal powers of τ we get the following:

$$\zeta_0 = \text{Bi}\tau, \tag{27}$$

$$\theta_{s0} = \frac{\text{Bi}^2\tau(1 + \text{Bi}\tau)}{[-1 + ((\text{Bi} - 1)\text{Bi}\tau)(\text{Bi}\tau\xi^2)]}. \tag{28}$$

It is relevant to mention here that the series expansion for the natural logarithm term in Eq. (25), $[\ln(1 - \zeta_0)]$ is used to assist with comparison of the coefficients.

3.1.2. First-order

In order to compute the first order coefficients, the first order expansion from Eq. (19) is substituted in Eqs. (14), (16). Comparing the terms of equal power of Ste yields the governing equations for the first order variables. For liquid phase we get:

$$(1 - \zeta_0)\frac{\partial^2\theta_{l1}}{\partial\eta^2} - 2\frac{\partial\theta_{l1}}{\partial\eta} = 0, \tag{29}$$

$$\frac{\partial\theta_{l1}}{\partial\eta}\Big|_{(1,\tau)} = 0, \quad \theta_{l1}(0, \tau) = 0.$$

For solid phase the expansion yields:

$$(1 - \xi\zeta_0)\frac{\partial^2\theta_{s1}}{\partial\xi^2} + \xi\zeta_1\frac{\partial^2\theta_{s0}}{\partial\xi^2} - 2\zeta_1\frac{\partial\theta_0}{\partial\xi} - 2\zeta_0\frac{\partial\theta_1}{\partial\xi} = 0, \tag{30}$$

$$\frac{\partial\theta_{s1}}{\partial\xi}\Big|_{(0,\tau)} - \zeta_1\text{Bi}(1 + \sqrt{\text{Ste}}\theta_{s1}(0, \tau)) = 0,$$

$$\theta_{s1}(1, \tau) = 0.$$

The interface equation becomes:

$$(1 - \zeta_0)\frac{\partial\theta_{s1}}{\partial\xi}\Big|_{(1,\tau)} - \zeta_1\frac{\partial\theta_{s0}}{\partial\xi}\Big|_{(1,\tau)} = \zeta_0(1 - \zeta_0)\frac{d\zeta_1}{d\tau} + \zeta_1(1 - 2\zeta_0)\frac{d\zeta_0}{d\tau}, \tag{31}$$

$$\zeta_1(0) = 0.$$

The solution for Eqs. (29)–(31) is computed as follows. For the liquid phase the solution is given by:

$$\theta_{l1} = 0. \tag{32}$$

Solving for the solid phase yields:

$$\theta_{s1} = \frac{\text{Bi}\zeta_1(1 - \xi + 2\text{Bi}\tau + \text{Bi}^2\xi_1\xi\tau\sqrt{\text{Ste}} - 2\text{Bi}\xi^2\tau - \text{Bi}^2\xi_1\xi^2\tau\sqrt{\text{Ste}} + 3\text{Bi}^2\xi\tau^2 - 3\text{Bi}^2\xi^2\tau^2)}{(1 + \text{Bi}\sqrt{\text{Ste}}\zeta_1 + \text{Bi}\tau)(-1 - \text{Bi}\tau + \text{Bi}^2\tau)(1 + \text{Bi}\xi\tau^2)}. \tag{33}$$

where, ζ_1 is an unknown and should be solved using Eq. (31). Analyzing the liquid phase outer solution we can see that it intuitively makes sense since for larger time steps the liquid temperature would reach the equilibrium freezing temperature T_f . The solution for the first order interface (ζ_1) is too complicated to compute, hence Eq. (33) cannot be closed.

The interface solution in the outer expansion yields realistic values for the total freezing time when compared with the experimental value of Hindmarsh et al. [7] for the parameters given in Table 1. However, the square root dependence of interface motion on time is not captured. In the next subsection we move on to the quasi-stationary approximation to find out if we can capture that trend both qualitatively and quantitatively.

3.2. Inner expansion

To capture the solution for time scales approaching zero it is imperative to use the stretched time coordinate T . Using this stretched time coordinate the dependent variables are transformed. These new variables, with an overbar, are defined as follows:

$$\begin{aligned} \bar{\theta}_s(\xi, T) &= \theta_s(\xi, \tau), \\ \bar{\theta}_l(\eta, T) &= \theta_l(\eta, \tau), \\ \bar{\zeta}(T) &= \zeta(\tau), \\ T &= \frac{\tau}{\text{Ste}}. \end{aligned} \tag{34}$$

Substituting the transformed variables from Eq. (34) in Eq. (14)–(16) yields:

$$\begin{aligned} \frac{\partial^2\bar{\theta}_l}{\partial\eta^2} - \frac{2}{1-\eta}\frac{\partial\bar{\theta}_l}{\partial\eta} &= \alpha\left[(1-\bar{\zeta})^2\frac{\partial\bar{\theta}_l}{\partial T} - (1-\xi)(1-\bar{\zeta})\frac{\partial\bar{\theta}_l}{\partial\eta}\frac{d\bar{\zeta}}{dT}\right], \\ \frac{\partial^2\bar{\theta}_s}{\partial\xi^2} - \frac{2\bar{\zeta}}{1-\bar{\zeta}\xi}\frac{\partial\bar{\theta}_s}{\partial\xi} &= \left[\bar{\zeta}^2\frac{\partial\bar{\theta}_s}{\partial T} - \bar{\zeta}\xi\frac{\partial\bar{\theta}_s}{\partial\xi}\frac{d\bar{\zeta}}{dT}\right]. \end{aligned} \tag{35}$$

The BCs and IC for solid and liquid phase:

$$\begin{aligned} \frac{\partial\bar{\theta}_l}{\partial\eta}\Big|_{(0,T)} = 0, \quad \bar{\theta}_l(0, T) = 0, \quad \bar{\theta}_l(\eta, 0) = \bar{\theta}_l, \\ \frac{1}{\bar{\zeta}}\frac{\partial\bar{\theta}_s}{\partial\xi}\Big|_{(0,T)} - \text{Bi}\bar{\theta}_s(0, T) = 0, \quad \bar{\theta}_s(1, T) = 1. \end{aligned} \tag{36}$$

The interface BC and IC transform to:

$$\begin{aligned} \text{Ste}\left[\frac{\partial\bar{\theta}_s}{\partial\xi}\Big|_{(1,T)} - \frac{\bar{\zeta}}{1-\bar{\zeta}}\frac{\partial\bar{\theta}_l}{\partial\eta}\Big|_{(0,T)}\right] &= \bar{\zeta}\frac{d\bar{\zeta}}{dT}, \\ \bar{\zeta}(0) &= 0. \end{aligned} \tag{37}$$

The following series expansion is proposed as a solution to Eqs. (35)–(37) with the stretched time scale T :

$$\begin{aligned} \bar{\theta}_s(\xi, T; \text{Ste}) &\sim \sum_{n=0}^N (\text{Ste})^{n/2}\bar{\theta}_{sn}(\xi, T), \\ \bar{\theta}_l(\eta, T; \text{Ste}) &\sim \sum_{n=0}^N (\text{Ste})^{n/2}\bar{\theta}_{ln}(\eta, T), \\ \bar{\zeta}(T; \text{Ste}) &\sim \sum_{n=0}^N (\text{Ste})^{n/2}\bar{\zeta}_n(T). \end{aligned} \tag{38}$$

3.2.1. Zero-order

Zero order solution is obtained by substituting the proposed series solution for $n = 0$ in Eqs. (35)–(37) and comparing the coefficients of Ste^0 . Starting from the interface equation and its initial condition we get:

$$\bar{\zeta}_0\frac{d\bar{\zeta}_0}{dT} = 0, \quad \bar{\zeta}_0(0) = 0, \tag{39}$$

which yields:

$$\bar{\zeta}_0(T) = 0. \tag{40}$$

With $\bar{\zeta}_0 = 0$ the resulting equation for solid phase is simplified considerably. For the solid phase the inner expansion yields:

$$\frac{\partial^2\bar{\theta}_{s0}}{\partial\xi^2} = 0, \quad \frac{\partial\bar{\theta}_{s0}}{\partial\xi}\Big|_{(0,T)} = 0, \quad \bar{\theta}_{s0}(1, T) = 1. \tag{41}$$

This yields the following result:

$$\bar{\theta}_{s0} = 1. \tag{42}$$

For the liquid phase the zero-order approximation yields the following set of equations:

$$\frac{\partial^2\bar{\theta}_{l0}}{\partial\eta^2} - \frac{2}{1-\eta}\frac{\partial\bar{\theta}_{l0}}{\partial\eta} - \alpha\frac{\partial\bar{\theta}_{l0}}{\partial T} = 0, \tag{43}$$

$$\frac{\partial\bar{\theta}_{l0}}{\partial\eta}\Big|_{(1,T)} = 0, \quad \bar{\theta}_{l0}(0, T) = 0, \quad \bar{\theta}_{l0}(\eta, 0) = \bar{\theta}_l. \tag{44}$$

Eq. (43) is a linear variable coefficient PDE which can be solved using separation of variables. Setting $\tilde{\eta} = 1 - \eta$ and re-arranging, Eq. (43) can be rewritten as:

$$\frac{1}{\tilde{\eta}}\frac{\partial^2(\tilde{\eta}\bar{\theta}_{l0})}{\partial\tilde{\eta}^2} = \alpha\frac{\partial\bar{\theta}_{l0}}{\partial T}. \tag{45}$$

Substitute $U(\tilde{\eta}, T) = \tilde{\eta}\bar{\theta}_{l0}(\tilde{\eta}, T)$ in Eq. (45) we get the following:

$$\frac{\partial^2 U}{\partial\tilde{\eta}^2} = \alpha\frac{\partial U}{\partial T}. \tag{46}$$

The BCs and the IC in Eq. (44) are transformed using the new variables as follows:

$$\bar{\theta}_{l0}(1, T) = 0 \rightarrow U(1, T) = 0, \tag{47}$$

$$\frac{\partial \bar{\theta}_{l0}}{\partial \eta} \Big|_{(0,T)} = 0 \rightarrow U(0, T) = 0, \quad (48)$$

$$U(\tilde{\eta}, 0) = \tilde{\eta} \theta_i. \quad (49)$$

Note that θ_{l0} is a function of $\tilde{\eta}$ and hence the boundary values are shifted accordingly. Eq. (48) is justified since the temperature at the center is finite as $\tilde{\eta} \rightarrow 0$. Using separation of variable technique we define:

$$U(\tilde{\eta}, T) = X(\tilde{\eta})Y(T). \quad (50)$$

Substituting Eq. (50) in Eq. (46) and employing separation of variable technique we get:

$$\frac{d^2 X}{d\tilde{\eta}^2} + X \beta_n^2 = 0, \quad (51)$$

$$\frac{dY}{dT} + \beta_n^2 \alpha Y = 0. \quad (52)$$

The need for the subscript 'n' in β_n^2 will become apparent later in the analysis. The general solutions for Eqs. (51), (52) are given as follows:

$$X = A \sin(\beta_n \tilde{\eta}) + B \cos(\beta_n \tilde{\eta}), \quad (53)$$

$$Y = \exp(-\alpha \beta_n^2 T). \quad (54)$$

The boundary conditions in Eqs. (47), (48) become:

$$X(1) = 0, \quad X(0) = 0. \quad (55)$$

Using Eq. (55) with Eq. (53) we get:

$$A = 0, \quad \sin(\beta_n) = 0, \quad (56)$$

which yields the following eigenvalues:

$$\beta_n = n\pi, \quad n = 1, 2, 3, \dots \quad (57)$$

Using these eigenvalues, the corresponding time factor from Eq. (54) becomes:

$$Y_n = \exp(-\alpha \beta_n^2 T). \quad (58)$$

Using the time factor, eigenvalues and the general solution, the total solution in Eq. (50) becomes:

$$U(\tilde{\eta}, T) = \sum_{n=1}^{\infty} a_n \exp(-\beta_n^2 \alpha T) \sin(\beta_n \tilde{\eta}). \quad (59)$$

Now, applying the initial condition as given in Eq. (49):

$$\tilde{\eta} \theta_i = \sum_{n=1}^{\infty} a_n \sin(\beta_n \tilde{\eta}). \quad (60)$$

In order to find the constant a_n we shall use the orthogonality of the sine functions. Multiplying both sides of the Eq. (60) by $\sin(m\pi\tilde{\eta})$ and applying orthogonality we get:

$$a_n = 2 \int_0^1 \tilde{\eta} \theta_i \sin(\beta_n \tilde{\eta}) d\tilde{\eta}. \quad (61)$$

Applying integration by parts on the integrand we get:

$$a_n = \theta_i \left(\frac{\sin \beta_n - \beta_n \cos \beta_n}{\beta_n^2} \right). \quad (62)$$

Which closes the Eq. (59) and the zero-order liquid solution. Converting U and $\tilde{\eta}$ to their original variables, the final solution is of the form:

$$\bar{\theta}_{l0}(\eta, T) = (1 - \eta) \theta_i \sum_{n=1}^{\infty} \exp(-\beta_n^2 \alpha T) \frac{\sin(\beta_n(1 - \eta))}{1 - \eta} \left(\frac{\sin \beta_n - \beta_n \cos \beta_n}{\beta_n^2} \right). \quad (63)$$

The matching for this solution was performed with the single-phase liquid sensible cooling solution (domain far from the interface) given by the Eq. (6) which yielded same results for the first 50 eigenvalues at the time approaching 0.

3.2.2. First-order

Substituting the series solution as proposed in Eq. (38) for $n = 1$ in Eqs. (35)–(37) and comparing the coefficients of $Ste^{1/2}$ we get the required equations and BCs. For solid phase this yields:

$$\frac{\partial^2 \bar{\theta}_{s1}}{\partial \xi^2} = 0, \quad (64)$$

$$\frac{\partial \bar{\theta}_{s1}}{\partial \xi} \Big|_{(0,T)} - \zeta_1 \text{Bi} [1 + \sqrt{Ste} \bar{\theta}_{s1}(0, T)] = 0, \quad (65)$$

$$\bar{\theta}_{s1}(1, T) = 0. \quad (66)$$

Solving Eq. (64) using the BCs, we get:

$$\bar{\theta}_{s1}(\xi, T) = \frac{\text{Bi} \bar{\zeta}_1 (\xi - 1)}{1 + \text{Bi} \sqrt{Ste} \bar{\zeta}_1}. \quad (67)$$

For the liquid phase the equation gets too complicated to compute. For the interface, comparing the terms of $Ste^{1/2}$ and Ste yields trivial solutions. Comparing the coefficients of $Ste^{3/2}$ we get:

$$\frac{\partial \bar{\theta}_{s1}}{\partial \xi} \Big|_{(1,T)} - \frac{\partial \bar{\theta}_{s0}}{\partial \xi} \Big|_{(1,T)} \bar{\zeta}_1 - \frac{\partial \bar{\theta}_{l0}}{\partial \eta} \Big|_{(0,T)} + \bar{\zeta}_1^2 \frac{d\bar{\zeta}_1}{dT} = 0, \quad (68)$$

where,

$$\frac{\partial \bar{\theta}_{s1}}{\partial \xi} \Big|_{(1,T)} = \frac{\bar{\zeta}_1 \text{Bi}}{\bar{\zeta}_1 \text{Bi} \sqrt{St} + 1}, \quad (69)$$

$$\frac{\partial \bar{\theta}_{s0}}{\partial \xi} \Big|_{(1,T)} = 0, \quad (70)$$

$$\frac{\partial \bar{\theta}_{l0}}{\partial \eta} \Big|_{(0,T)} = \sum_{n=1}^{\infty} a_n \exp\left(-\frac{\beta_n^2 T}{\alpha}\right) \frac{\sin(\beta_n) - \beta_n \cos(\beta_n)}{\beta_n} \quad (71)$$

Eq. (71) yields a very long governing equation for Eq. (68) because of the infinite Eigenvalue terms. In order to simplify the equation only the first term of Eq. (71) is taken. This assumption is justified because the derivative of the term is being computed at the interface where even a single eigenvalue results in a relatively accurate solution for liquid temperature as given by Eq. (63). Substituting Eq. (69), (70) and the first term of Eq. (71) in Eq. (68) and simplifying:

$$\bar{\zeta}_1 \frac{d\bar{\zeta}_1}{dT} - \frac{\text{Bi}}{\bar{\zeta}_1 \text{Bi} \sqrt{St} + 1} + \frac{2\theta_i}{\pi} \exp\left(\frac{-\pi^2 T}{\alpha}\right) = 0, \quad (72)$$

$$\bar{\zeta}_1 = 0. \quad (73)$$

Both Bi and Ste are $\ll 1$ for the values given in Table 1. Hence the denominator of the second term can be ignored. The resulting equation is:

$$\bar{\zeta}_1 \frac{d\bar{\zeta}_1}{dT} - \text{Bi} + \frac{2\theta_i}{\pi} \exp\left(\frac{-\pi^2 T}{\alpha}\right) = 0. \quad (74)$$

Solving for $\bar{\zeta}_1$ using Eqs. (73), (74) we get:

$$\bar{\zeta}_1 = \frac{\sqrt{4\theta_i \left[-1 + \exp\left(\frac{-\pi^2 T}{\alpha}\right)\right] \alpha + 2\text{Bi}\pi^3 T}}{\pi^{\frac{3}{2}}}. \quad (75)$$

As shown in Eq. (75) the square root dependence of the interface position on the time has been captured in this expansion. Another important dependence captured here is the effect of droplet's initial temperature and Biot number on the interface position.

4. Numerical modeling

This study uses the enthalpy–porosity fixed grid method to numerically compute the phase-change behavior of the water droplet. Enthalpy–porosity method as pioneered by Voller et al. [41] and Brent et al. [44], assumes that the phase-change interface has a finite thickness and treats it as a pseudo-porous media. The method precludes the need to satisfy the energy conservation condition at the phase-change interface and instead adjusts the nodal latent heat content of the cells in

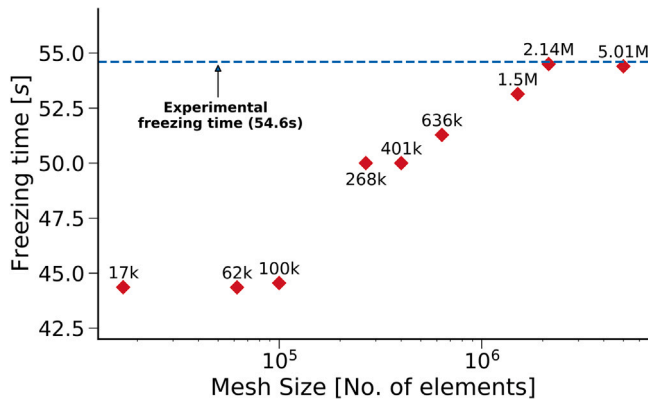


Fig. 2. Mesh sensitivity analysis of the droplet freezing model for $a = 0.78$ mm. The dashed blue line shows the experimental freezing time taken from Hindmarsh et al. [7].

the computational domain according to the cell temperature to account for absorption or evolution of the latent heat.

For this study a 3-D model of the droplet is created and meshed in ANSYS design modeler and ANSYS Mesher, respectively. For the 3-D droplet, an unstructured tetrahedral mesh was used with the average aspect ratio and skewness of 1.17 and 0.11 respectively. Both of these metrics are well within the recommended limits of < 5 and < 0.33 for aspect ratio and skewness respectively. To ensure that the numerical results are mesh insensitive, a mesh independence study was conducted for 10 different mesh sizes ranging from 17k to 5 million cells. The results from the mesh sensitivity analysis are shown in Fig. 2. As illustrated in the figure, the 0.78 mm radius droplet discretized into around 2 million nodes gives a good accuracy with the experimental freezing time and is thus used for the numerical studies.

For the simulations the momentum equations within the droplet are disabled whereas only the energy equation is computed. The governing equations along with the relevant boundary conditions are solved using a finite volume solver as implemented in Ansys Fluent 18.1. Conservation of energy equation computed by the solver is given by:

$$\frac{\partial}{\partial t} \left[\rho_s (1 - \gamma) H_s + \rho_l \gamma (H_l + L) \right] = \nabla \cdot [k_d(T) \nabla T], \quad (76)$$

where, H_s and H_l are the sensible enthalpies [J/kg] of the solid and liquid phases, respectively and L is the Latent heat of fusion. The enthalpies are computed using the following expressions:

$$H_s = \int_{T_{ref}}^T c_{p,s}(T) dT, \quad (77)$$

$$H_l = \int_{T_{ref}}^T c_{p,l}(T) dT.$$

$k_d(T)$ in Eq. (76) is the mixture thermal conductivity and is computed by the expression:

$$k_d(T) = (1 - \gamma)k_s(T) + \gamma k_l(T). \quad (78)$$

Here k_s and k_l are the thermal conductivity in the solid and liquid phase respectively. The enthalpy term in Eq. (76) switches its expression for different phases according to the value of liquid fraction which is given by:

$$\gamma = \begin{cases} 0 & T < T_{sol}, \\ \frac{T - T_{sol}}{T_{liq} - T_{sol}} & T_{sol} \leq T \leq T_{liq}, \\ 1 & T > T_{liq}. \end{cases} \quad (79)$$

In Eq. (79) T_{sol} and T_{liq} are the solidus and liquidus temperature of the mixture and define the thickness of the mushy zone. Expressions of the temperature dependent thermal properties, k_s , k_l , ρ_s , ρ_l , $c_{p,s}$,

Table 2

Physical properties of water and ice used for the enthalpy–porosity model.

Property	Expression	Unit
k_l	$-1.111 \times 10^{-7} T^3 + 9.115 \times 10^{-5} T^2 - 0.02301 T + 2.31$	W/(m K)
k_s	$-8.272 \times 10^{-18} T^3 + 5.714 \times 10^{-5} T^2 - 0.03922 T + 8.659$	W/(m K)
ρ_l	$4.889 \times 10^{-3} T^3 - 0.04831 T^2 + 15.51 T - 629.2$	kg/m ³
ρ_s	$-0.0005333 T^3 + 0.4043 T^2 - 102.2 T - 9527$	kg/m ³
$c_{p,l}$	$-0.001556 T^3 - 1.397 T^2 - 418.3 T + 4.599 \times 10^4$	J/(kg K)
$c_{p,s}$	$-3.042 \times 10^{-17} T^3 - 0.02 T^2 + 16.03 T - 832.3$	J/(kg K)
μ_l	$9.447 \times 10^4 \exp(-0.06897 T) + 0.09804 \exp(-0.01622 T)$	W/(m K)
T_{liq}	273.25	K
T_{sol}	273.15	K
σ	1.38065×10^{-23}	m ² kg/(s ² K)
ϵ	0.97	-
L_v	2500	kJ/kg

$c_{p,l}$ were incorporated in the simulation using a User Defined Function (UDF) routine written in C. The temperature dependent properties in the enthalpy–porosity method allow us to accurately model the thermal diffusivity which proves to be a critical physical parameter in determining the accuracy of the freezing times. More discussion on this is conducted in the verification and the validation subsection. The expressions for the thermal properties used are listed in Table 2.

The solver uses the numerical approach outlined by Swaminathan & Voller [45] to solve the energy equation and liquid volume fraction, γ , iteratively. The diffusion term in Eq. (76) is discretized using a second order central difference scheme whereas the transient term is discretized using the first order explicit forward marching scheme.

4.1. Boundary conditions

The BCs and the IC for the Eq. (76) are given as:

$$\begin{aligned} -k_d \frac{\partial T}{\partial r} \Big|_{(a,t)} &= h_{eq}(T(a,t) - T_\infty), \\ \frac{\partial T}{\partial r} \Big|_{(0,r)} &= 0, \\ T(r,0) &= T_i. \end{aligned} \quad (80)$$

In order to incorporate the evaporation, radiation, and heat losses through thermocouple as measured in the experiments conducted by Hindmarsh et al. [7], a modified, equivalent, heat transfer coefficient (h_{eq}) is defined as follows:

$$h_{eq} = h_{conv} + h_{rad} + h_{eva} + h_{therm}. \quad (81)$$

h_{conv} contributes to about 80% of the total heat transfer rate and is calculated through the Ranz–Marshall Nusselt number correlation [46] which is given as follows:

$$Nu = \frac{h_{conv} d}{k} = 2 + 0.6 Re^{1/2} Pr^{1/3}. \quad (82)$$

Here, Re and Pr and Reynolds number and Prandtl number, respectively, for the water droplet traveling with the velocity, v , relative to the air. For the base case the values of these parameters are listed in Table 1. To calculate the respective heat transfer coefficients for radiation, evaporation and thermocouple heat loss we use the steps laid out as follows:

- Calculate the heat flux for each of the three mechanisms;
- Identify a suitable reference temperature differential. In this study we use $T_i - T_\infty$; and
- Use the equation, $h_{rad,eva,therm} = \dot{q}_{rad,eva,therm} / (T_i - T_\infty)$, to calculate the respective equivalent heat transfer rate.

In reality, the heat transfer rates are a function of droplet temperature and will change iteratively with the temperature evolution of the droplet. However, the contribution of the last three terms in Eq. (81) is one order of magnitude less than h_{conv} . Hence using a constant heat flux over a fixed, reference range of temperature is justified.

The equation listed in step (iii) requires calculation of a reference individual heat flux. The radiation heat flux is calculated using the following expression:

$$\dot{q}_{rad} = \epsilon \sigma (T_i^4 - T_\infty^4). \quad (83)$$

Here, ϵ is the emissivity of ice and σ is the Boltzmann constant. For heat flux due to evaporation we use the equation:

$$\dot{q}_{eva} = \dot{m}_{eva}(L_v), \quad (84)$$

where,

$$\dot{m}_{eva} = \frac{h_m}{\bar{R}} \left(\frac{P_{sw}}{T} \right). \quad (85)$$

The mass transfer coefficient (h_m) is calculated using the Ranz Marshall Sherwood correlation [7], which is given as:

$$Sh = \frac{2h_m d}{D_{ab}} = 2 + 0.6Re^{1/2} Sc^{1/3}, \quad (86)$$

where Schmidt number, Sc , equals $\mu_a / \rho_a D_{ab}$. The expression for P_{sw} in Eq. (86) is extracted from the paper by Murphy & Koop [47]. The heat loss due to thermocouple is calculated by the methodology and data as outlined by Hindmarsh [7]. The reader is referred to that study for more details.

5. Results and discussion

After laying out the results from the perturbation series solution and defining the outline of the numerical methodology used in this study, we explore their results further in this section. We start by presenting the verification of our analytical model with our enthalpy–porosity numerical model and the numerical results from the literature [16]. In order to justify the verification of the sharp-interface front tracking analytical method with the fixed-grid pseudo porous media numerical method, we keep the liquidus and solidus temperature difference to be within 0.1 K. Our perturbation series solution and numerical model is also validated with the experimental data of Hindmarsh et al. [7], where we present the results of the temperature profile evolution with time for the cases of with and without supercooling.

To demonstrate the accuracy and applicability of our perturbation series solution and numerical model we have computed the temperature profile and freezing times of the water droplet for the spray freezing application. The temperature profile has been computed by combining the solution methodologies for the stages of liquid sensible cooling (2.2), phase-change (2.3) and solid sub-cooling (2.4), respectively. The freezing time is calculated in two steps. First the interface location expression ξ for $N = 1$ in Eq. (38) is evaluated. Next, ζ is set to 1 (complete freezing) and the corresponding time is calculated which is referred to as the freezing time hereafter. For verification and validation purposes, the non-dimensional variables have been re-dimensionalized using the appropriate expressions.

The following subsection presents and discusses the validation and verification of the perturbation series solution.

5.1. Verification and validation

In this subsection, we present the verification and validation of our perturbation series solution and enthalpy–porosity model with the numerical and experimental data in the literature, respectively. Fig. 3 shows the comparison of the results from our perturbation series solution with our enthalpy–porosity numerical model and the hybrid numerical–analytical results from Dehghani et al. [16] (without supercooling). The comparison shows that enthalpy–porosity model and perturbation series solution match to within a maximum error of 3% in predicting the freezing time of the droplet and temperature profiles in liquid and solid phases. The results are also observed to be in good agreement with Dehghani's model. The slight discrepancy

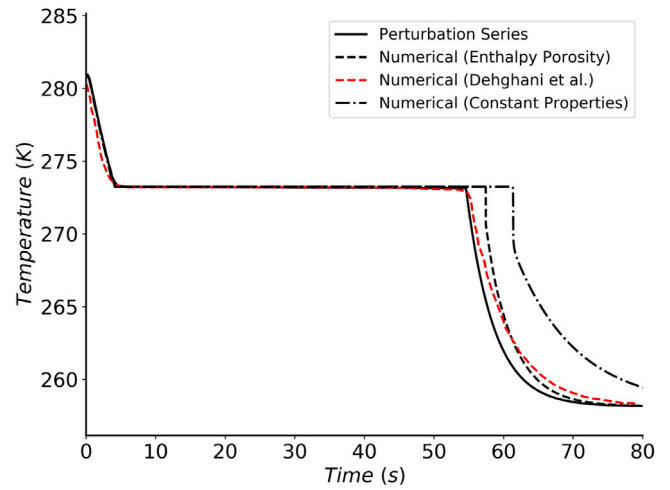


Fig. 3. Verification of the temperature evolution at the center of the droplet of radius 780 μm . The results are compared from the numerical results of Dehghani et al. [16].

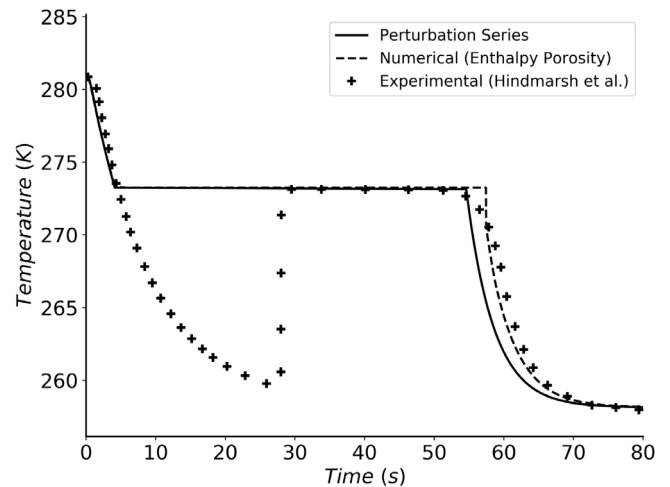


Fig. 4. Validation of the temperature evolution at the center of the droplet of radius 780 μm without supercooling. The experimental results are taken from Hindmarsh et al. [7].

observed between our numerical and analytical model can be attributed to the difference in phase-change modeling approach and the use of temperature dependent thermal properties for the enthalpy–porosity model. This hypothesis is verified by conducting numerical simulation for the constant properties case (as shown by the dashed–dotted line) in Fig. 3 which over predicts the solution as compared to the temperature-dependent properties case.

Fig. 4 presents the validation of the perturbation series solution and enthalpy porosity method (without supercooling) with the experimental results of Hindmarsh et al. [7]. Both the perturbation series solution and enthalpy–porosity model compare well with the experimental freezing time and temperature profile for the sensible cooling stage in liquid and solid phases. The numerical model matches to within 1% accuracy with the experimental freezing time and temperature profile of the solid sub-cooling stage. The perturbation series solution slightly under predicts the freezing time and consequently the solid sub-cooling. However, it is still within 4% accuracy which constitutes as a good approximation for a series solution.

From Figs. 3 and 4, it is clear that the perturbation series and numerical solution were not able to predict the supercooling and consequent nucleation of the liquid phase. This is because the Stefan

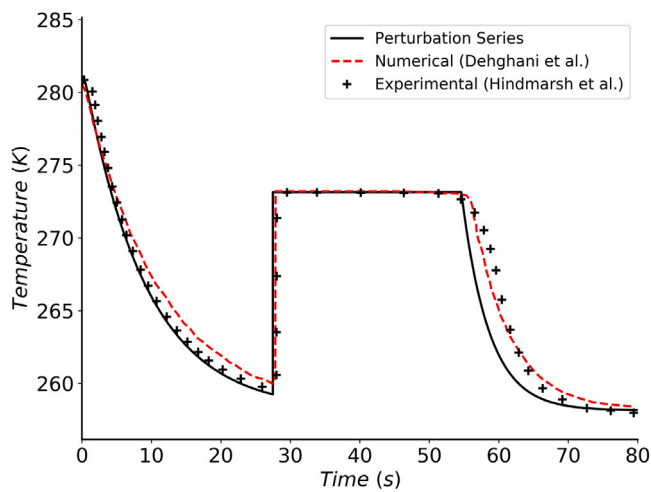


Fig. 5. Validation of the temperature evolution at the center of the droplet of radius 780 μm with supercooling. Experimental results taken from Hindmarsh et al. [7] and numerical results from Dehghani et al. [16].

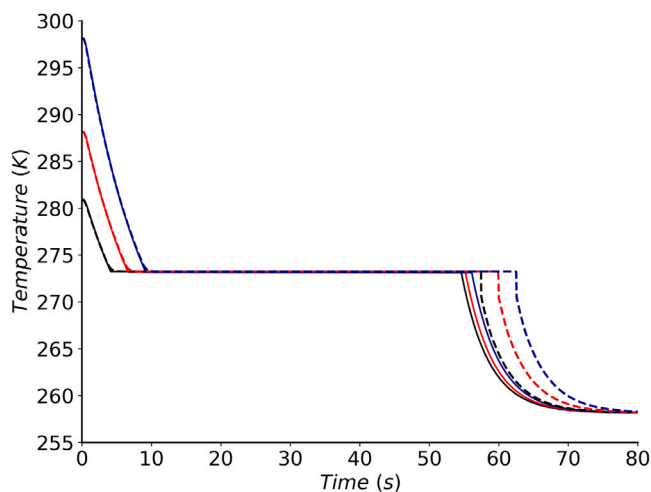


Fig. 6. Temperature evolution for 3 different initial droplet temperatures using perturbation series (solid lines) and enthalpy–porosity (dashed lines). The initial temperatures studied here are 280.85 K (black color), 288.15 K (red color) and 298.15 K (blue color).

problem models equilibrium freezing and thus does not take into account the non-equilibrium thermodynamics associated with nucleation and dendritic growth. However, if nucleation temperature is known a priori from experimental data and the recalescence is assumed to raise the temperature of the melt instantly to the freezing temperature after nucleation, the perturbation series solution developed here can be modified to include supercooling. To achieve that we constrained the liquid sensible cooling model developed in Section 2.2 to “super-cool” till nucleation. The results are shown in Fig. 5.

Fig. 5 shows a good agreement of droplet temperature by the perturbation series solution for all the freezing stages. The decaying profile of the liquid sub-cooling in the perturbation series analysis matches to within 2% with the experimental results. For the solid phase the decaying rate of the temperature profile agrees well with Dehghani’s model and experimental profiles. However the analytical model under predicts the solid-subcooling temperature to within 5% accuracy (with regards to the time to reach a particular temperature). The freezing time and the time to reach thermal equilibrium with the environment are however predicted within 2% accuracy.

Table 3

Different cases of Bi, Ste and T_i for the parametric study.

Parameters	Cases No.	Case values	T_∞	Radius	Velocity	h_{eq}
	–	–	K	μm	m/s	W/(m K)
Bi	Case 1	0.0286	258.15	150	0.42	318.01
	Case 2	0.0421	258.15	312.5	0.681	224.26
	Case 3	0.0562	258.15	475	0.97	197.14
Ste	Case 1	0.0189	270.15	780	0.54	127
	Case 2	0.0754	261.15	780	0.54	127
	Case 3	0.1257	253.15	780	0.54	127
T_i [K]	Case 1	280.85	258.15	780	0.54	127
	Case 2	288.15	258.15	780	0.54	127
	Case 3	298.15	258.15	780	0.54	127

Following the verification and validation we compare the impact of initial temperature, Biot number and Stefan number on the temperature and liquid fraction profile prediction for both perturbation series results and numerical models. The range of Bi and Ste used is computed using practical values for the geometrical and operational parameters such as droplet radius, air temperature and velocity of air. Bi is a direct function of the radius of the droplet and heat transfer coefficient. The heat transfer coefficient, in turn, depends on the radius itself and the velocity of the air flowing over the droplet. Ste, on the other hand, is a function of the air temperature. The complete grid of the cases evaluated and the corresponding operating parameters are given in Table 3. For Bi, the droplet radius is varied by taking the extremes and mean from the diameter distribution from a study by Santangelo [48]. For the rest of the parameters evaluated, the diameter is taken to be the same as the base case of Hindmarsh et al. [7] for the sake of continuity. The temperature and liquid fraction evolution of the droplet have been studied for three different cases of Bi and Ste. For Ste, the values for T_∞ are taken from the data based on seasonal variation of temperature during the winter time in Canada [49]. These cases cover the extreme values of the droplet radius, velocity and ambient air temperature for the spray freezing application.

5.2. Effect of initial temperature

Most of the asymptotic models developed in the literature are unable to capture the effect of initial droplet temperature on the sensible-cooling and freezing times of droplet. In our perturbation series expansion we were able to portray that effect (Eq. (75)). The speed of the interface in two-phase Stefan problems has often been simplified or reduced to one-phase problems, which is insensitive to the initial liquid temperature. McCue et al. [12] proved that the liquid phase contributed exponentially small terms to the interface motion for small Stefan numbers, and Brosa Planella et al. [40] assumed that the amount of supercooling had no influence on the location of interface. However, both cases solve for a Dirichlet boundary condition and the latter also considers mass diffusion (also categorized as extended Stefan problem). In this study, the initial liquid temperature and amount of supercooling can play a more significant role, since a convective boundary condition is prescribed.

Fig. 6 shows how the perturbation series model and the enthalpy–porosity model predicts the temperature evolution for different initial droplet temperatures. For these scenarios the Bi and Ste are kept to be at the same values as the base case (Table 1). Fig. 6 depicts that the initial temperature affects the temperature profile during the sensible cooling phase and the freezing time of the droplet. Both the perturbation solution and enthalpy–porosity model predict the liquid sensible cooling stage accurately and overall compare well to within 10% across the range. It is also observed from Fig. 6 that the effect of initial temperature on sensible cooling profile is more pronounced as compared to the freezing time. This observation is consistent with

the results from the hybrid analytical–numerical model of Deghani et al. [16].

5.3. Effect of Biot number

Figs. 7–9 show the results for temperature and liquid fraction profiles for cases 1, 2 and 3 of the Biot numbers as presented in Table 3. The Ste for 3 different cases of Bi has been kept constant at 0.094 (same as base case). As for the freezing time predictions, it can be noted from Figs. 7–9(a) that the perturbation series over predicts the freezing time for all cases of Bi by around 10%. The temperatures for the liquid sub-cooling phase, however, are predicted to within 1% agreement of the numerical results as shown by the insets. The relatively larger discrepancy for the freezing times can be associated with the assumption of using phase dependent properties only for the analytical solution. The hypothesis is verified by comparing the enthalpy–porosity model results of temperature averaged physical properties with the perturbation solution. As shown in the verification curve (Fig. 3), the constant properties curve (shown as the dash dot line) over-predicts the freezing time. The discrepancy can be physically explained by the slow heat diffusivity prediction for temperature averaged physical properties as compared to using the fully temperature dependent physical properties.

The liquid fraction profiles as depicted in Figs. 7–9 show the evolution of the phase-change process within different points inside a freezing droplet for different cases of Bi . The figures also show that the freezing time increases monotonically with the Bi (and the droplet diameter). Comparing the 3 figures, it is evident that the spacing between the liquid fraction values at the “equally spaced” spatial points is not uniform. This shows that the interface motion is non-linear. We, in fact, know this from the literature and our perturbation series solution to be true. According to the literature, the interface motion varies non-linearly with time. A direct corollary of this non-linear variation is the increase in interface velocity as it approaches the center of the droplet. In Figs. 7–9(b), this is mirrored by the sharp change in the liquid fraction profile at $r = 0$.

Figs. 7–9 also show the comparison between the perturbation series solution (solid lines) and enthalpy–porosity (dashed) model. The difference between these two approaches is evident from the trend. Since the perturbation series assumes a sharp interface between solid and liquid phases, the liquid fraction from the perturbation series solution exhibit a step function behavior regardless of the location within the droplet or the cooling rate of the droplet. Enthalpy–porosity model, on the other hand, exhibits different behaviors for different locations and cooling conditions. As observed from Figs. 7–9, for the outer layer of the droplet, it exhibits sharp change between the phases due to a direct exposure to the cooling source. However, as the freezing penetrates inwards, the shift between phases becomes less abrupt. This behavior is expected since the enthalpy–porosity model assumes the phase-change to occur within a finite, pseudo-porous mushy zone.

5.4. Effect of Stefan number

Figs. 10–12(a) show the temperature profile for 3 different cases of Ste as given in Table 3. The insets show the comparison for the liquid sub-cooling stage which depict a good agreement between analytical and numerical results (within 1%). This trend is in-line with what is observed for the case of different Bi . Comparison of the freezing times for three different cases of Ste show that the freezing time decreases non-linearly with an increase in Ste . This result is intuitive since low Ste corresponds to low cooling potential of the surrounding air resulting in slow cooling rate of the droplet.

It can also be observed from Figs. 10–12(a) that the perturbation series solution under predicts the freezing times for low Ste as compared to the enthalpy–porosity model. However, with an increase in the Ste the agreement becomes better. Overall, for 3 different cases of Ste , the agreement between perturbation series and enthalpy porosity is within

8%. It is important to note here that even though the Ste is the highest for Fig. 12, however in relative terms it is still low and thus rendering the asymptotic approximation valid.

Figs. 10–12(b) show the profiles of liquid fraction at different locations within the freezing droplets as predicted by perturbation series and enthalpy–porosity model. As depicted by these figures, the trend shows that the relative freezing time between the outer surface and the center of the droplet is lowest for case 1 of Ste . Fig. 10(b) also shows that the liquid fraction at all points gradually changes in case of low sensible heat stimuli (270.15 K) which is a departure from the trend shown by all the other 5 cases investigated in this study. These differences in the relative freezing times between outer surface and the center of the droplet for different Stefan numbers (and thus different sensible heat stimuli) can be useful in design considerations of Phase-Change Materials (PCMs), where it is important to determine the local freezing times for efficient design.

It is also important to note that for low sensible heat stimuli (Fig. 12), the droplet liquid fraction at the center does not change sharply for enthalpy–porosity model, whereas the perturbation series solution shows a sharp change. This is one of the shortcoming of perturbation approach as it assumes a sharp interface between solid and liquid phases regardless of the cooling potential of the source.

6. Conclusion

This study develops, verifies and validates a novel perturbation series model for low Ste and radially symmetric droplet that evaluates the phase-change behavior of a two-phase Stefan problem. The effects of initial temperature and convective boundary conditions were captured in the perturbation series model which have not previously been studied in the literature. Perturbation method is advantageous since it is a rigorous mathematical homogenization method that allows for obtaining the average behavior of the complex physical phenomena as a closed-form solution. This allows for less computational time in conducting parametric and design optimization studies as compared to numerical methods. The series solution developed validates to within 4% accuracy for temperature profile at the droplet center and freezing time, even with the first two terms of the perturbation series only, thus demonstrating the advantage of developing asymptotic solution. These perturbation series results developed for a finite, radially symmetric problem are useful as they can be used as a subgrid model in a direct numerical simulation for the process of crystal growth in a droplet [50] to significantly speed up the computational process of crystal growth simulations.

Our study also develops and validates an enthalpy–porosity fixed grid phase-change model to investigate droplet freezing. Results from the perturbation series and numerical model are further evaluated for different cases of droplet initial temperature, Biot and Stefan numbers calculated based on the realistic geometric and operational properties of water droplets in spray freezing application. The analytical solution is able to predict liquid and solid sub-cooling accurately for all conditions. However, it is within 1%–10% accurate in predicting freezing times depending on the Bi and Ste .

The solution tends to over predict freezing times for different cases of Bi (and smaller droplet sizes) whereas it under predicts the freezing times for different Ste . Results show that the discrepancy between analytical and numerical results is more sensitive to the variability of Stefan number as opposed to Bi (For the given range). The dependency of initial droplet temperature on freezing times and sensible-cooling regime is also demonstrated to good effect. Since the overall cases of Bi and Ste are low for the spray freezing application, this shows that the perturbation solutions developed in the limit of low Ste can be a quick, useful tool to evaluate the thermal behavior for such systems during the phase-change process. However, the study also highlights

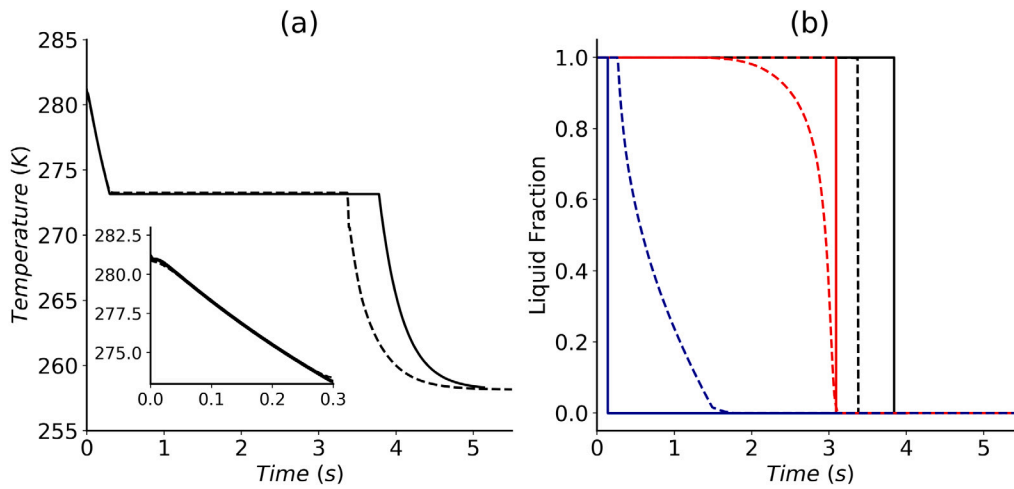


Fig. 7. Center temperature (a) and liquid fraction (b) evolution at $Bi = 0.0286$. The comparison between numerical solution (dashed lines) and perturbation series solution (solid lines) is presented. In the subplot (b) different colors correspond to different points within the droplet. The black color corresponds to droplet center ($r = 0$), where as the red and blue colors show the liquid fraction evolution at $r = 0.6 a$ and $r = a$, respectively.

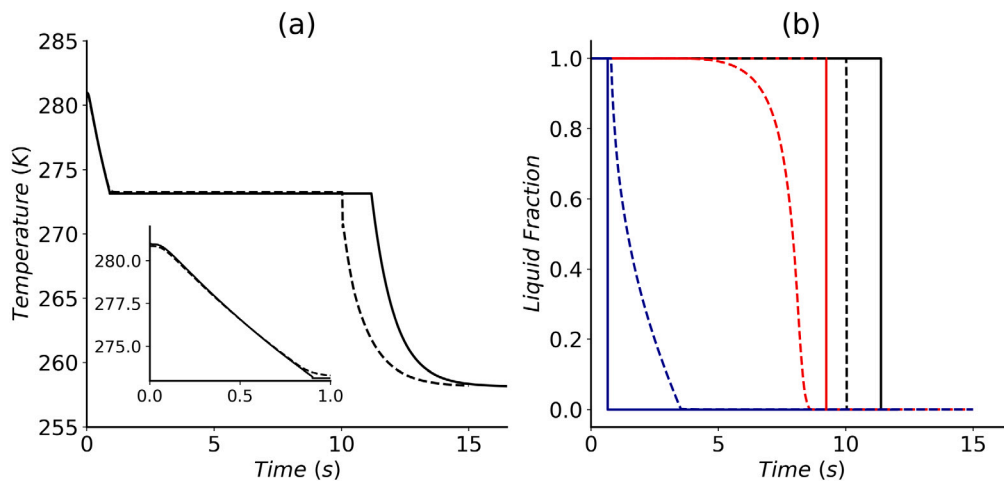


Fig. 8. Center temperature (a) and liquid fraction (b) evolution at $Bi = 0.0421$. The comparison between numerical solution (dashed lines) and perturbation series solution (solid lines) is presented. In the subplot (b) different colors correspond to different points within the droplet. The black color corresponds to droplet center ($r = 0$), where as the red and blue colors show the liquid fraction evolution at $r = 0.6 a$ and $r = a$, respectively.

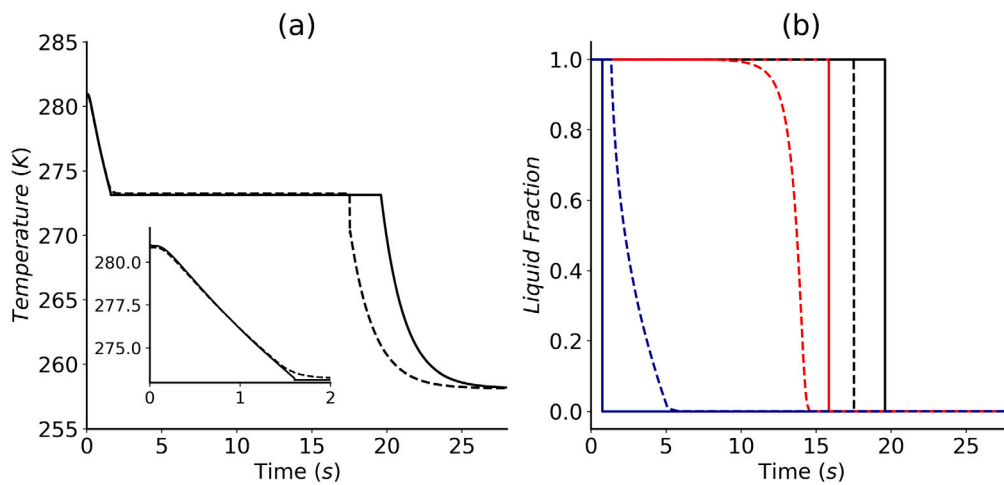


Fig. 9. Center temperature (a) and liquid fraction (b) evolution at $Bi = 0.0562$. The comparison between numerical solution (dashed lines) and perturbation series solution (solid lines) is presented. In the subplot (b) different colors correspond to different points within the droplet. The black color corresponds to droplet center ($r = 0$), where as the red and blue colors show the liquid fraction evolution at $r = 0.6 a$ and $r = a$, respectively.

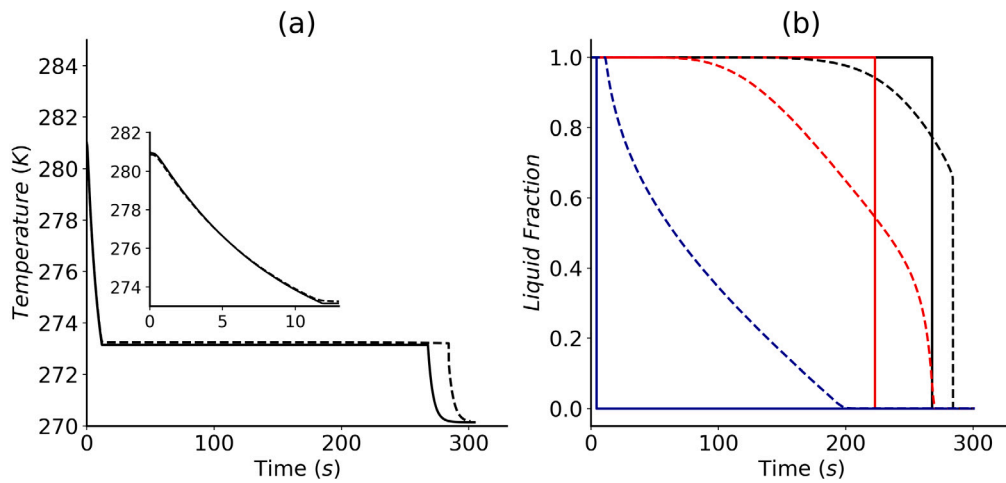


Fig. 10. Center temperature (a) and liquid fraction (b) evolution at $Ste = 0.0189$. The comparison between numerical solution (dashed lines) and perturbation series solution (solid lines) is presented. In the subplot (b) different colors correspond to different points within the droplet. The black color corresponds to droplet center ($r = 0$), where as the red and blue colors show the liquid fraction evolution at $r = 0.6 a$ and $r = a$, respectively.

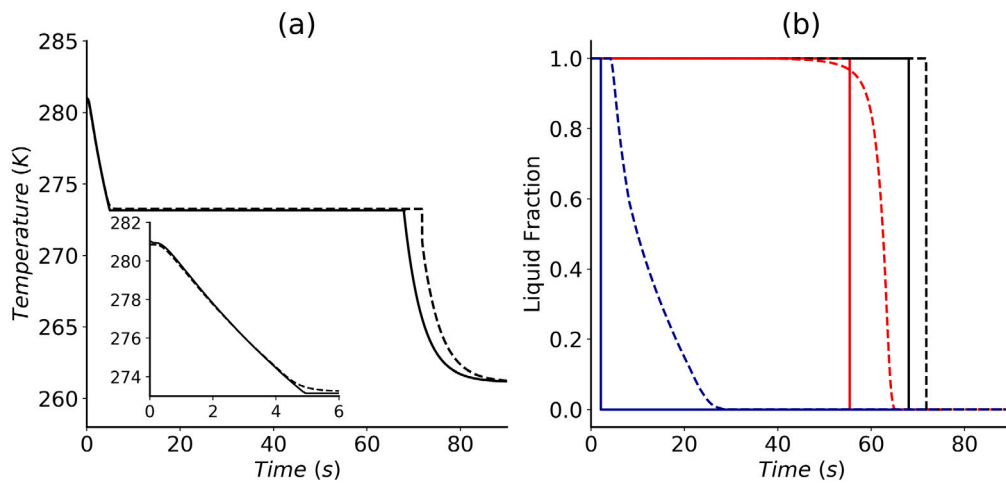


Fig. 11. Center temperature (a) and liquid fraction (b) evolution at $Ste = 0.0754$. The comparison between numerical solution (dashed lines) and perturbation series solution (solid lines) is presented. In the subplot (b) different colors correspond to different points within the droplet. The black color corresponds to droplet center ($r = 0$), where as the red and blue colors show the liquid fraction evolution at $r = 0.6 a$ and $r = a$, respectively.

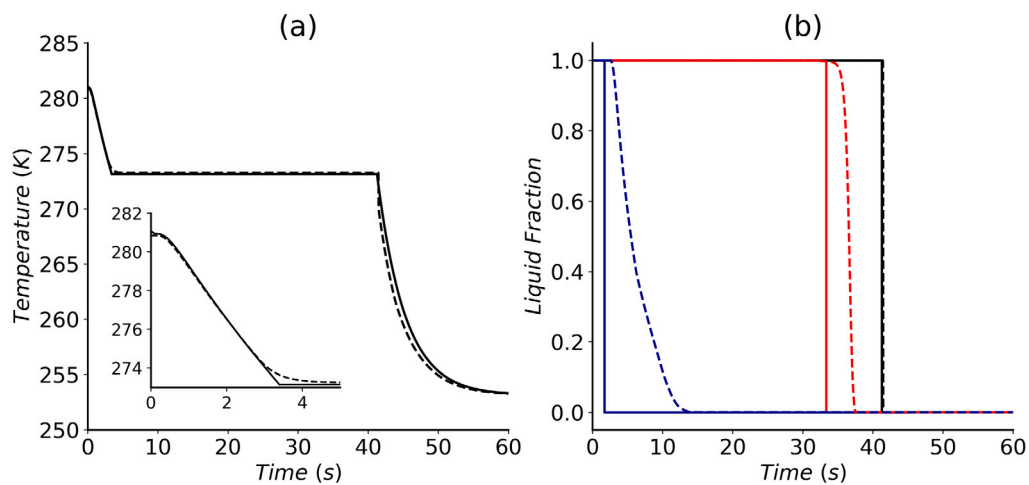


Fig. 12. Center temperature (a) and liquid fraction (b) evolution at $St = 0.126$. The comparison between numerical solution (dashed lines) and perturbation series solution (solid lines) is presented. In the subplot (b) different colors correspond to different points within the droplet. The black color corresponds to droplet center ($r = 0$), where as the red and blue colors show the liquid fraction evolution at $r = 0.6 a$ and $r = a$, respectively.

the limitations of perturbation series solution in predicting liquid fractions within different locations in the droplet since it assumes a sharp phase-change interface.

Our perturbation series model is able to predict the supercooling of the liquid droplet, provided the nucleation temperature is known a priori. An interesting avenue of the future work in this area would be to develop a separate framework for incorporating nucleation and non-equilibrium thermodynamics of the crystallization process and integrate it with the perturbation series solution of the equilibrium Stefan problem. This would help with a continuous prediction of the supercooling and recalescence phenomena for the droplet freezing process that would yield in a uniformly valid solution at all times.

Declaration of competing interest

The authors declare that they have no known competing financial interests or personal relationships that could have appeared to influence the work reported in this paper.

Acknowledgments

The first author would like to extend his gratitude to McGill Engineering Doctoral Award (MEDA), Canada and Fonds de recherche du Quebec – Nature et technologies (FRQNT), Canada – Bourses de doctorat (B2X) for supporting this research. The simulations for this study was conducted at the HPC facility under Calcul-Quebec and Compute-Canada with contribution from CFI-JELF.

References

- J.C. Liao, K.C. Ng, Effect of ice nucleators on snow making and spray freezing, *Ind. Eng. Chem. Res.* 29 (3) (1990) 361–366.
- A. Lauber, A. Kiselev, T. Pander, P. Handmann, T. Leisner, Secondary ice formation during freezing of levitated droplets, *J. Atmos. Sci.* 75 (8) (2018) 2815–2826.
- S. Akhtar, A. Madiseh, A. Sasmito, Numerical investigation of a novel phase-change renewable energy system for underground mine heating and cooling, in: *Refrigeration Science and Technology*, 2018, <http://dx.doi.org/10.18462/iir.pcm.2018.0007>.
- J. Stachulak, Ventilation strategy and unique air conditioning at Inco Limited, 1988, pp. 3–9.
- S. Wanning, R. Sauerkrup, A. Lamprecht, Pharmaceutical spray freeze drying, *Int. J. Pharm.* 488 (1–2) (2015) 136–153.
- I.B. Sebastião, B. Bhatnagar, S. Tchessalov, S. Ohtake, M. Plitzko, B. Luy, A. Alexenko, Bulk dynamic spray freeze-drying part 1: Modeling of droplet cooling and phase change, *J. Pharm. Sci.* 108 (6) (2019) 2063–2074.
- J. Hindmarsh, A. Russell, X. Chen, Experimental and numerical analysis of the temperature transition of a suspended freezing water droplet, *Int. J. Heat Mass Transfer* 46 (7) (2003) 1199–1213.
- S.Y. Hundre, P. Karthik, C. Anandharamkrishnan, Effect of whey protein isolate and β -cyclodextrin wall systems on stability of microencapsulated vanillin by spray-freeze drying method, *Food Chem.* 174 (2015) 16–24.
- M.-J. Liu, Z.-Q. Zhu, L.-W. Fan, Z.-T. Yu, An experimental study of inward solidification of nano-enhanced phase change materials (nepcm) inside a spherical capsule, in: *ASME 2016 Heat Transfer Summer Conference*, American Society of Mechanical Engineers Digital Collection, 2016.
- D. Erdemir, Numerical investigation of thermal performance of geometrically modified spherical ice capsules during the discharging period, *Int. J. Energy Res.* 43 (9) (2019) 4554–4568.
- D.L. Feltham, J. Garside, Analytical and numerical solutions describing the inward solidification of a binary melt, *Chem. Eng. Sci.* 56 (7) (2001) 2357–2370.
- S.W. McCue, B. Wu, J.M. Hill, Classical two-phase stefan problem for spheres, *Proc. Royal Soc. A: Math. Phys. Eng. Sci.* 464 (2096) (2008) 2055–2076.
- D. Riley, F. Smith, G. Poots, The inward solidification of spheres and circular cylinders, *Int. J. Heat Mass Transfer* 17 (12) (1974) 1507–1516.
- L.M. Jiji, S. Weinbaum, Perturbation solutions for melting or freezing in annular regions initially not at the fusion temperature, *Int. J. Heat Mass Transfer* 21 (5) (1978) 581–592.
- M. Asker, H. Ganjehsarabi, M.T. Coban, Numerical investigation of inward solidification inside spherical capsule by using temperature transforming method, *Ain Shams Eng. J.* 9 (4) (2018) 537–547.
- A. Dehghani-Sani, S. MacLachlan, G. Naterer, Y. Muzychka, R. Haynes, V. Enjilela, Multistage cooling and freezing of a saline spherical water droplet, *Int. J. Therm. Sci.* 147 (2020) 106095.
- S.L. Mitchell, T.G. Myers, Application of standard and refined heat balance integral methods to one-dimensional stefan problems, *SIAM Rev.* 52 (1) (2010) 57–86, <http://dx.doi.org/10.1137/080733036>, arXiv:<https://doi.org/10.1137/080733036>.
- S. Nandi, Y. Sanyasiraju, An adi based body-fitted method for stefan problem in irregular geometries, *Int. J. Therm. Sci.* 157 (2020) 106473, <http://dx.doi.org/10.1016/j.ijthermalsci.2020.106473>.
- M. Mahamudur Rahman, H. Hu, H. Shabgard, P. Boettcher, Y. Sun, M. McCarthy, Experimental characterization of inward freezing and melting of additive-enhanced phase-change materials within millimeter-scale cylindrical enclosures, *J. Heat Transfer* 138 (7) (2016).
- S. Wildeman, S. Sterl, C. Sun, D. Lohse, Fast dynamics of water droplets freezing from the outside in, *Phys. Rev. Lett.* 118 (8) (2017) 084101.
- C. Chan, F. Tan, Solidification inside a sphere—an experimental study, *Int. Commun. Heat Mass Transfer* 33 (3) (2006) 335–341.
- K. Cho, S. Choi, Thermal characteristics of paraffin in a spherical capsule during freezing and melting processes, *Int. J. Heat Mass Transfer* 43 (17) (2000) 3183–3196.
- E. Assis, G. Ziskind, R. Letan, Numerical and experimental study of solidification in a spherical shell, *J. Heat Transfer* 131 (2) (2009).
- H.S. Carslaw, J.C. Jaeger, *Conduction of Heat in Solids*, second ed., Clarendon Press, Oxford, 1959, 1959.
- Rubinštein, *The Stefan Problem*, Vol. 8, American Mathematical Soc., 2000.
- L.N. Tao, The exact solutions of some stefan problems with prescribed heat flux, *J. Appl. Mech.* 48 (4) (1981) 732–736, <http://dx.doi.org/10.1115/1.3157724>.
- Y. Zhou, K. Wang, Similarity solution for one-dimensional heat equation in spherical coordinates and its applications, *Int. J. Therm. Sci.* 140 (2019) 308–318.
- A.H. Nayfeh, *Perturbation Methods*, John Wiley Sons, 2008.
- M. Van Dyke, *Perturbation Methods in Fluid Mechanics/Annotated Edition*, NASA STI/Recon Technical Report A 75, 1975.
- A. Aziz, T.Y. Na, *Perturbation Methods in Heat Transfer*, 212, Hemisphere Publishing Corp., Washington, DC, 1984, p. 1984.
- A. Aziz, V.J. Lunardini, Perturbation techniques in phase change heat transfer, *Appl. Mech. Rev.* 46 (2) (1993) 29–68, <http://dx.doi.org/10.1115/1.3120319>.
- F. Feuillebois, A. Lasek, P. Creisemeas, F. Pigeonneau, A. Szaniawski, Freezing of a subcooled liquid droplet, *J. Colloid Interface Sci.* 169 (1) (1995) 90–102, <http://dx.doi.org/10.1006/jcis.1995.1010>.
- S. Tabakova, F. Feuillebois, S. Radev, Freezing of a supercooled spherical droplet with mixed boundary conditions, *Proc. Royal Soc. A: Math. Phys. Eng. Sci.* 466 (2116) (2009) 1117–1134.
- R. Pedroso, G. Domoto, Inward spherical solidification—solution by the method of strained coordinates, *Int. J. Heat Mass Transfer* 16 (5) (1973) 1037–1043.
- M. Prud'Homme, T.H. Nguyen, D.L. Nguyen, A heat transfer analysis for solidification of slabs, cylinders, and spheres, *J. Heat Transfer* 111 (3) (1989) 699–705.
- M. Parang, D. Crocker, B. Haynes, Perturbation solution for spherical and cylindrical solidification by combined convective and radiative cooling, *Int. J. Heat Fluid Flow* 11 (2) (1990) 142–148.
- A. Soward, A unified approach to stefan's problem for spheres and cylinders, *Proc. R. Soc. Lond. Ser. A Math. Phys. Eng. Sci.* 373 (1752) (1980) 131–147.
- K. Stewartson, R. Waechter, On stefan's problem for spheres, *Proc. R. Soc. Lond. Ser. A Math. Phys. Eng. Sci.* 348 (1655) (1976) 415–426.
- A. Kucera, J.M. Hill, On inward solidifying cylinders and spheres initially not at their fusion temperature, *Int. J. Non-Linear Mech.* 21 (1) (1986) 73–82, [http://dx.doi.org/10.1016/0020-7462\(86\)90014-4](http://dx.doi.org/10.1016/0020-7462(86)90014-4).
- F. Brosa Planella, C.P. Please, R.A. Van Gorder, Extended stefan problem for the solidification of binary alloys in a sphere, *European J. Appl. Math.* (2020) 1–38, <http://dx.doi.org/10.1017/S095679252000011X>.
- V.R. Voller, C.R. Swaminathan, Eral source-based method for solidification phase change, *Numer. Heat Transfer B* 19 (2) (1991) 175–189, <http://dx.doi.org/10.1080/10407799108944962>.
- A. Mills, *Basic Heat Mass Transfer*, Prentice Hall, 1999.
- P. Virtanen, R. Gommers, T.E. Oliphant, M. Haberland, T. Reddy, D. Cournapeau, E. Burovski, P. Peterson, W. Weckesser, J. Bright, S.J. van der Walt, M. Brett, J. Wilson, K. Jarrod Millman, N. Mayorov, A.R.J. Nelson, E. Jones, R. Kern, E. Larson, C. Carey, Í. Polat, Y. Feng, E.W. Moore, J. VanderPlas, D. Laxalde, J. Perktold, R. Cimrman, I. Henriksen, E.A. Quintero, C.R. Harris, A.M. Archibald, A.H. Ribeiro, F. Pedregosa, P. van Mulbregt, S. Contributors, SciPy 1.0: Fundamental algorithms for scientific computing in Python, *Nature Methods* 17 (2020) 261–272, <http://dx.doi.org/10.1038/s41592-019-0686-2>.
- A. Brent, V. Voller, K. Reid, Enthalpy-porosity technique for modeling convection–diffusion phase change: application to the melting of a pure metal, *Numer. Heat Transfer A* 13 (3) (1988) 297–318.

- [45] C.R. Swaminathan, V.R. Voller, A general enthalpy method for modeling solidification processes, *Metall. Trans. B* 23 (5) (1992) 651–664, <http://dx.doi.org/10.1007/BF02649725>.
- [46] F.P. Incropera, *Fundamentals of Heat and Mass Transfer*, John Wiley & Sons, Inc., Hoboken, NJ, USA, 2006.
- [47] D.M. Murphy, T. Koop, Review of the vapour pressures of ice and supercooled water for atmospheric applications, *Q. J. R. Meteorol. Soc.: A J. Atmos. Sci. Appl. Meteorol. Phys. Oceanogr.* 131 (608) (2005) 1539–1565.
- [48] P.E. Santangelo, Characterization of high-pressure water-mist sprays: Experimental analysis of droplet size and dispersion, *Exp. Therm Fluid Sci.* 34 (8) (2010) 1353–1366, <http://dx.doi.org/10.1016/j.expthermflusci.2010.06.008>.
- [49] M.A. Alzoubi, S. Akhtar, M. Fong, A.P. Sasmito, Characterization of an open-loop seasonal thermal energy storage system, *Energy Procedia* 142 (2017) 3401–3406.
- [50] F.I. Dragomirescu, K. Eisenschmidt, C. Rohde, B. Weigand, Perturbation solutions for the finite radially symmetric stefan problem, *Int. J. Therm. Sci.* 104 (2016) 386–395, <http://dx.doi.org/10.1016/j.ijthermalsci.2016.01.019>.